Electronic Supplementary Material (ESI) for Dalton Transactions.

Electronic Supplementary Information

Core-shell and heterostructured silver-nickel nanocatalysts fabricated by γ-radiation induced synthesis for oxygen reduction in alkaline media

Yi Yang[1*], Gerard Montserrat-Sisó[2], Björn Wickman[2], Pavel Anatolyevich Nikolaychuk[3], Inna L. Soroka[1*]

[1]*Applied Physical Chemistry, Department of Chemistry, School of Engineering Sciences in Chemistry, Biotechnology and Health, KTH Royal Institute of Technology, S-100 44 Stockholm, Sweden*

[2]*Chemical Physics, Department of Physics, Chalmers University of Technology, 412 96 Gothenburg, Sweden*

[3]*Institute of Environmental and Agricultural Biology (X-BIO), University of Tyumen, 625003 Tyumen, Russian Federation*

[*]*Corresponding Authors*

Content

1. Details of material synthesis

For ionizing radiation induced synthesis, Cs-137 gamma source, MDS Nordion 1000 Elite, was used. The total absorbed dose was controlled by irradiation duration. The dose rate estimated with ferrous sulfate dosimetry was 0.15 Gy s^{-1}. The nanoparticles were synthesized using metal salt solutions with 5 mM of corresponding precursor concentration. IPA was added as OH radicals' scavenger, and PVA was used as a surfactant. Prior to irradiation all mixtures were purged with N_2 (99.999 % purity, Linde) for 30 min and sealed with a septum in glass vials. The irradiation time was 40 hours for all samples. It corresponds to the total irradiation dose of 21.6 kGy. The initial pH of the solution was about 5.5, after irradiation pH decreased to about 3. The obtained Ni precipitates were separated from solutions by using a magnet in the glovebox under Ar atmosphere (oxygen content < 0.1 ppm). The Ag-contained precipitates were separated by centrifugation at 8000 rpm for 15 min, then washed with IPA/Milli-Q water three times and dispersed in IPA.

2. Material characterization and analysis details

2.1 Details of XPS fitting

For the curve fitting of both Ni-2p and Ag-3d a standard Shirley background was used, together with a Gaussian-Lorentzian peak profiles. All peaks emerging from core level photoelectrons were fitted using a doublet with a ratio suitable for the orbital (2:1 for Ni-2p and 2:3 for Ag-3d). The binding energy values were allowed to shift by ± 0.3 eV to account for errors associated with referencing to adventitious carbon. The study of the oxidation state of the Ni 2p core level spectrum is known to be compromised by the presence of secondary peaks emerging from multiplet splitting, plasmon loss structures and satellite peaks overlapping with the primary structure of the spectrum. Overlapping of the high binding energy satellite and plasmon-loss Ni structures with the $2p_{1/2}$ photoelectron lines makes the curve fitting by doublets very problematic. The deconvolution is focused on the fitting of the $2p_{3/2}$ lines to ensure secondary photoelectrons are not taken into account for the quantification. Similarly, Ag-3d peaks also show the presence of plasmon-loss structures at higher binding energies, but they do not interfere with Ag primary peaks. All these secondary peaks were fitted with singlets and were not taken into account for the quantification of the oxidation states. To further prove the existence of the oxidation states found by fitting Ni and Ag peaks, deconvolution of the O-1s peak could also be carried out. This option has been dismissed due to the presence of too many oxygenated compounds in Ni and Ag, as well as adsorbed oxygen. The study of Ag-3d spectra is much less problematic due to the sufficient energy difference between primary and secondary peaks. However, the close proximity of all its oxide peaks can make the peak assignment deceptive.

2.2 Details of ICP-OES analysis

To obtain an accurate electrochemically active surface area (ECSA) value, the actual amount of catalyst on modified glassy carbon (GC) electrode was quantified by ICP-OES before and after electrochemical tests. Specifically, 100 µL of freshly prepared nanoparticle suspension was taken and digested with 2 mL aqua regia (prepared using HCl and HNO_3) for 24 hours. The solution was then diluted to 10 times as the testing solution. After the electrochemical test, the working electrode was disassembled from the RDE rotating lever and immersed into a glass vial containing 0.5 ml H_2O. Catalyst layer on GC electrodes was then exfoliated via ultra-sonication and re-dispersed in 0.5 mL H_2O. 2 mL aqua regia was then added and digested for 24 hours. The

analyzing solution sample was then prepared similarly with 10 times dilution. Standard ICP solutions of each element were prepared and measured prior to the real samples to calibrate and obtain the standard curves. The composition of bimetallic Ag-Ni samples and metal amount on GC are shown in Table S5.

3. Calculation of potential–pH diagram of Ni-Ag system

The chemical and electrochemical equilibria of the Ni–Ag–NO_3^-–AcO^-–H_2O system is calculated based on the thermodynamic activities of nickel, Ag, nitrate, and acetate ions in aqueous solutions at T=298.15 K, atmospheric pressure, and at solution pH ranging from 1 to 6. The partial pressure of methane was considered to be equal to 2×10^{-6} bar that corresponds to the average concentration of methane in the air.[1] The standard Gibbs energy of formation of nickel hydride Ni_2H was taken from the literature.[2]

3.1 Phase equilibria in the Ag–Ni system at 25 °C.

According to the phase diagram of the Ag–Ni system,[3] silver and nickel are only very slightly soluble in each other in the solid state. Both solid solutions of Ag in (Ni) and Ni in (Ag) have the same face-centered cubic crystal structure.

The maximum solid solubility at 298 K might be estimated by considering the equilibrium condition of equality of chemical potentials of both silver and nickel in both solutions:

$$\begin{cases} \mu_{Ag}^{(Ag)} = \mu_{Ag}^{(Ni)}, \\ \mu_{Ni}^{(Ag)} = \mu_{Ni}^{(Ni)}, \end{cases}$$

where $\mu_i^{(j)}$ is the chemical potential of component i in the phase (j), the subscript i denotes the component (Ag or Ni), and the superscript (j) denotes the solvent in the solid solution ((Ag) or (Ni)).

Any chemical potential might be expressed as:

$$\mu_i^{(j)} = \mu_i^{0,(j)} + R \cdot T \cdot ln\, x_i^{(j)} + \mu_i^{E,(j)},$$

where $\mu_i^{0,(j)}$ is the chemical potential of the pure substance i in the phase (j). $x_i^{(j)}$ is the mole fraction of the component i in the phase (j), and $\mu_i^{E,(j)}$ is the excess chemical potential of the component i in the phase (j).

Because both solid solutions have the same crystal structure, the chemical potentials of both pure silver and nickel in both phases are equal to each other:

$$\begin{cases} \mu_{Ag}^{0,(Ag)} = \mu_{Ag}^{0,(Ni)}, \\ \mu_{Ni}^{0,(Ag)} = \mu_{Ni}^{0,(Ni)}. \end{cases}$$

Moreover, the excess Gibbs energies of both phases are also the same:

$$G^{E,(Ag)} = G^{E,(Ni)} = G^E.$$

According to ref.[3], the excess Gibbs energy of the fcc solid solution in the Ag – Ni system might be expressed in form of Redlich-Kister power series:[4]

$$G^E = x_{Ag} \cdot x_{Ni} \cdot \left(L_1 \cdot (x_{Ag} - x_{Ni}) + L_0\right).$$

From this expression the excess chemical potentials of the components might be expressed as follows:

$$\mu_{Ag}^E = A_1 \cdot x_{Ni}^2 + B_1 \cdot x_{Ni}^3,$$

$$\mu_{Ni}^E = A_2 \cdot x_{Ag}^2 + B_2 \cdot x_{Ag}^3.$$

where,

$A_1 = L_0 + 3 \cdot L_1$,

$A_2 = L_0 - 3 \cdot L_1$,

$B_1 = -4 \cdot L_1$,

$B_2 = 4 \cdot L_1$.

According to the data of ref.[3]:

$L_0 = (3{,}1 \cdot T + 54620{,}4),\ ^{J}/_{mol}$,

$L_1 = 2800,\ ^{J}/_{mol}$.

By substituting aforementioned equations into the equilibrium condition, the following system of equation might be derived:

$$\begin{cases} R \cdot T \cdot \ln x_{Ag}^{(Ag)} + A_1 \cdot \left(x_{Ni}^{(Ag)}\right)^2 + B_1 \cdot \left(x_{Ni}^{(Ag)}\right)^3 = R \cdot T \cdot \ln x_{Ag}^{(Ni)} + A_1 \cdot \left(x_{Ni}^{(Ni)}\right)^2 + B_1 \cdot \left(x_{Ni}^{(Ni)}\right)^3, \\ R \cdot T \cdot \ln x_{Ni}^{(Ag)} + A_1 \cdot \left(x_{Ag}^{(Ag)}\right)^2 + B_1 \cdot \left(x_{Ag}^{(Ag)}\right)^3 = R \cdot T \cdot \ln x_{Ni}^{(Ni)} + A_1 \cdot \left(x_{Ag}^{(Ni)}\right)^2 + B_1 \cdot \left(x_{Ag}^{(Ni)}\right)^3, \\ x_{Ag}^{(Ag)} + x_{Ni}^{(Ag)} = 1, \\ x_{Ag}^{(Ni)} + x_{Ni}^{(Ni)} = 1. \end{cases}$$

Solving this system at T = 298,15 K gives the following values:

$$\begin{cases} x_{Ni}^{(Ag)} = 6{,}004 \cdot 10^{-11}, \\ x_{Ag}^{(Ag)} \approx 1, \\ x_{Ag}^{(Ni)} = 5{,}758 \cdot 10^{-10}, \\ x_{Ni}^{(Ni)} \approx 1. \end{cases}$$

The activities of the components of both solid solutions might be calculated as follows:

$R \cdot T \cdot ln\ a_{Ag} = R \cdot T \cdot ln\ x_{Ag} + A_1 \cdot x_{Ni}^2 + B_1 \cdot x_{Ni}^3$,

$R \cdot T \cdot ln\ a_{Ni} = R \cdot T \cdot ln\ x_{Ni} + A_2 \cdot x_{Ag}^2 + B_2 \cdot x_{Ag}^3$.

According to calculations:

$$\begin{cases} a_{Ni}^{(Ag)} \approx 1, \\ a_{Ag}^{(Ag)} \approx 1, \\ a_{Ag}^{(Ni)} \approx 1, \\ a_{Ni}^{(Ni)} \approx 1. \end{cases}$$

Both solid solutions exhibit strong positive deviations from ideal behavior.

As calculations show, at the standard temperature, the solid solubility of both components in each other is vanishingly small. Even despite nanosized particles usually are more soluble than bulk phases, this solubility might be definitely neglected. Therefore, both solid silver and nickel will be treated as pure compounds in further calculations.

3.2 The oxides of silver and nickel

Silver forms a variety of oxides, namely, Ag_2O, Ag_2O_2 and Ag_2O_3. Nickel forms a continuous series of oxides with the formula NiO_x, where $1 \le x \le 2$. Silver and nickel could form a variety of mixed oxides,[5] including $AgNiO_2$, Ag_2NiO_2 and $Ag_3Ni_2O_4$. However, there is a lack of thermodynamic information concerning these compounds, and, therefore, the ternary silver–nickel oxides will be excluded from further thermodynamic calculations.

3.3 Thermodynamic data on silver and nickel oxides and aqueous species

Compound	The standard Gibbs energy of formation, $^{J}/_{mol}$

	Ref.[6]	Ref.[7]	Ref.[8]	Ref.[9]	Value used in further calculations
Ni^{2+} (aq)	–45 800	–46 400	–	–45 600	–45 800
NiO (s)	–211 700	–	–212 300	–211 700	–211 700
$NiOH^{+}$ (aq)	–228 500	–227 300	–226 500	–227 600	–227 300
$Ni(OH)_2$ (aq)	–	–	–399 400	–360 200	–399 400
$Ni(OH)_2$ (s)	–457 100	–446 900	–457 600	–447 200	–457 600
$Ni(OH)_3^-$ (aq)	–590 500	–	–	–	–590 500
Ni_2OH^{3+} (aq)	–268 200	–	–268 300	–	–268 300
$Ni_4(OH)_4^{4+}$ (aq)	–974 600	–	–972 600	–	–972 600
$HNiO_2^-$ (aq)	–	–350 000	–	–	–350 000
NiOOH (aq)	–	–316 900	–	–	–316 900
$Ni(OAc)^{+}$ (aq)	–	–	–	–422 900	–422 900
$Ni(OAc)_2$ (aq)	–	–	–	–801 900	–801 900
Ag^{+} (aq)	–	77 100	77 100	77 100	77 100
Ag^{2+} (aq)	–	268 600	–	269 000	268 600
AgO^{-} (aq)	–	–22 600	–	–	–22 600
Ag_2O (s)	–	–11 300	–11 400	–11 200	–11 300
Ag_2O_2 (s)	–	27 600	–	27 600	27 600
Ag_2O_3 (s)	–	–	–	121 400	121 400
$AgNO_3$ (aq)	–	–33 500	–	–32 500	–33 500
AgOAc (s)	–	–	–	–307 700	–307 700
AgOAc (aq)	–	–296 200	–	–296 400	–296 200
$Ag(OAc)_2^-$ (aq)	–	–	–	–665 200	–665 200
AgOH (aq)	–	–	–93 000	–92 000	–93 000
$Ag(OH)_2^-$ (aq)	–	–	–258 300	–260 200	–258 300
NO_3^- (aq)	–110 800	–110 900	–	–108 700	–110 800
HNO_2 (aq)	–	–55 700	–	–50 600	–55 700
NO_2^- (aq)	–	–36 800	–	–32 200	–36 800
NH_4^+ (aq)	–	–79 500	–	–79 300	–79 500
NH_4OH (aq)	–	–264 000	–	–263 700	–264 000
AcO^{-} (aq)	–	–369 500	–	–369 300	–369 500
AcOH (aq)	–	–396 600	–	–396 500	–396 500
CH_4 (g)	–	–50 600	–	–50 500	–50 600

3.4 Thermodynamic activities of aqueous species

The extended Debye – Hückel equation parameters:[10]

T = 298.15 K.

$$\varepsilon = 87,74 - 0,4008 \cdot (T - 273,15) +$$
$$+9,398 \cdot 10^{-4} \cdot (T - 273,15)^2 + 1,41 \cdot 10^{-6} \cdot (T - 273,15)^3 = 78,3294.$$

$$A = \frac{1,825 \cdot 10^6}{(\varepsilon \cdot T)^{\frac{3}{2}}} = \frac{1,825 \cdot 10^6}{(78,3294 \cdot 298,15)^{\frac{3}{2}}} = 0,5114 \ {}^{L^{\frac{1}{2}}}\!/_{mol^{\frac{1}{2}}},$$

$$B = \frac{5,029 \cdot 10^{11}}{(\varepsilon \cdot T)^{\frac{1}{2}}} = \frac{5,029 \cdot 10^{11}}{(78,3294 \cdot 298,15)^{\frac{1}{2}}} = 3,291 \cdot 10^9 \ {}^{L^{\frac{1}{2}}}\!/_{m \cdot mol^{\frac{1}{2}}}.$$

The electrostatic radii of the individual ions:[11]

Ion	a_i, Å
Ag^+ (aq)	2,5
Ni^{2+} (aq)	3,0
NO_3^-(aq)	3,0
AcO^- (aq)	4,5

The ionic strength of the solution:

$$I = \frac{z^2_{Ni^{2+}} \cdot c_{Ni^{2+}} + z^2_{AcO^-} \cdot c_{AcO^-} + z^2_{Ag^+} \cdot c_{Ag^{2+}} + z^2_{NO_3^-} \cdot c_{NO_3^-}}{2} =$$
$$= \frac{4 \cdot 0,005 \text{ M} + 1 \cdot 0,010 \text{ M} + 1 \cdot 0,005 \text{ M} + 1 \cdot 0,005 \text{ M}}{2} = 0,020 \text{ M}$$

The thermodynamic activities of the ions:

$$\lg \gamma_{Ni^{2+}} = -0,5114 \ {}^{L^{\frac{1}{2}}}\!/_{mol^{\frac{1}{2}}} \cdot (+2)^2 \cdot \frac{\sqrt{0,020 \ {}^{mol}\!/_{L}}}{1 + 3,291 \cdot 10^9 \ {}^{L^{\frac{1}{2}}}\!/_{m \cdot mol^{\frac{1}{2}}} \cdot 3,0 \cdot 10^{-10} \text{ m} \cdot \sqrt{0,020 \ {}^{mol}\!/_{L}}} = -0,254,$$

$$\gamma_{Ni^{2+}} = 10^{-0,254} = 0,557,$$

$$a_{Ni^{2+}} = 0,005 \frac{\text{mol}}{\text{L}} \cdot 0,557 = 0,00279 \frac{\text{mol}}{\text{L}}.$$

$$\lg \gamma_{AcO^-} = -0,5114 \ {}^{L^{\frac{1}{2}}}\!/_{mol^{\frac{1}{2}}} \cdot (-1)^2 \cdot \frac{\sqrt{0,020 \ {}^{mol}\!/_{L}}}{1 + 3,291 \cdot 10^9 \ {}^{L^{\frac{1}{2}}}\!/_{m \cdot mol^{\frac{1}{2}}} \cdot 4,5 \cdot 10^{-10} \text{ m} \cdot \sqrt{0,020 \ {}^{mol}\!/_{L}}} = -0,0598,$$

$$\gamma_{AcO^-} = 10^{-0,0598} = 0,871,$$

$$a_{AcO^-} = 0,010 \frac{\text{mol}}{\text{L}} \cdot 0,871 = 0,00871 \frac{\text{mol}}{\text{L}}.$$

$$\lg \gamma_{Ag^+} = -0,5114 \ {}^{L^{\frac{1}{2}}}\!/_{mol^{\frac{1}{2}}} \cdot (+1)^2 \cdot \frac{\sqrt{0,020 \ {}^{mol}\!/_{L}}}{1 + 3,291 \cdot 10^9 \ {}^{L^{\frac{1}{2}}}\!/_{m \cdot mol^{\frac{1}{2}}} \cdot 2,5 \cdot 10^{-10} \text{ m} \cdot \sqrt{0,020 \ {}^{mol}\!/_{L}}} = -0,0648,$$

$$\gamma_{Ag^+} = 10^{-0,0648} = 0,861,$$

$$a_{Ag^+} = 0,005 \frac{\text{mol}}{\text{L}} \cdot 0,861 = 0,0043 \frac{\text{mol}}{\text{L}}.$$

$$\lg \gamma_{NO_3^-} = -0{,}5114 \, {}^{\frac{1}{L^2}}\!/_{mol^{\frac{1}{2}}} \cdot (-1)^2 \cdot \frac{\sqrt{0{,}020 \, {}^{mol}\!/_{L}}}{1 + 3{,}291 \cdot 10^9 \, {}^{\frac{1}{L^2}}\!/_{m \cdot mol^{\frac{1}{2}}} \cdot 3{,}0 \cdot 10^{-10} \, m \cdot \sqrt{0{,}020 \, {}^{mol}\!/_{L}}} = -0{,}0637,$$

$$\gamma_{NO_3^-} = 10^{-0{,}0637} = 0{,}864,$$

$$a_{NO_3^-} = 0{,}005 \, \frac{mol}{L} \cdot 0{,}864 = 0{,}00432 \, \frac{mol}{L}.$$

3.5 Chemical equilibria in aqueous solution

3.5.1. Equilibria involving silver-acetate complexation

For the equilibrium

$CH_3COOH\ (aq) \rightleftharpoons CH_3COO^-\ (aq) + H^+\ (aq)$

the pK_a value is equal to 4,76.[12] This means that at pH < 4,76 the predominant form in solution is $CH_3COOH\ (aq)$, and at pH > 4,76 the acetate-ion $CH_3COO^-\ (aq)$ predominates.

For the equilibrium

$CH_3COOAg\ (s) \rightleftharpoons CH_3COO^-\ (aq) + Ag^+\ (aq)$

the solubility product value K_{sp} is equal to 1,94.[12] Using the activities of silver and acetate ions, calculated afore, one might calculate that

$$a_{CH_3COO^-\ (aq)} \cdot a_{Ag^+\ (aq)} = 0{,}00871 \, {}^{mol}\!/_{L} \cdot 0{,}0043 \, {}^{mol}\!/_{L} = 1{,}78 \cdot 10^{-5} \, {}^{mol^2}\!/_{L^2} < K_{sp}(CH_3COOAg\ (s)),$$

and, consequently, silver acetate does not precipitate at the reaction conditions. Solid silver acetate is excluded from further consideration.

For the equilibria

$$\begin{cases} Ag^+\ (aq) + CH_3COO^-\ (aq) \rightleftharpoons CH_3COOAg\ (aq), \\ CH_3COOAg\ (aq) + CH_3COO^-\ (aq) \rightleftharpoons Ag(CH_3COO)_2^-\ (aq), \\ H^+\ (aq) + CH_3COO^-\ (aq) \rightleftharpoons CH_3COOH\ (aq) \end{cases}$$

the standard Gibbs energies of reaction and the corresponding equilibrium constants might be calculated from the data, presented afore.

The activities of the species are related to each other according to the following equations:

$$\begin{cases} \dfrac{a_{CH_3COOAg\ (aq)}}{a_{Ag^+\ (aq)} \cdot a_{CH_3COO^-\ (aq)}} = 5{,}021 \, {}^{L}\!/_{mol}, \\ \dfrac{a_{Ag(CH_3COO)_2^-\ (aq)}}{a_{CH_3COOAg\ (aq)} \cdot a_{CH_3COO^-\ (aq)}} = 1{,}470 \cdot 10^{-5} \, {}^{L}\!/_{mol}, \\ \dfrac{a_{CH_3COOH\ (aq)}}{a_{H^+\ (aq)} \cdot a_{CH_3COO^-\ (aq)}} = 5{,}594 \cdot 10^4 \, {}^{L}\!/_{mol}, \\ a_{Ag^+\ (aq)} + a_{CH_3COOAg\ (aq)} + a_{Ag(CH_3COO)_2^-\ (aq)} = 0{,}0043 \, {}^{mol}\!/_{L}, \\ a_{CH_3COOH\ (aq)} + a_{CH_3COO^-\ (aq)} + a_{CH_3COOAg\ (aq)} + 2 \cdot a_{Ag(CH_3COO)_2^-\ (aq)} = 0{,}00871 \, {}^{mol}\!/_{L}. \end{cases}$$

By solving this system of equations, the dependencies of thermodynamic activities of ions might be expressed as the functions of pH value. These dependencies are shown in the diagram below.

The activity of the complex ion $Ag(CH_3COO)_2^-\ (aq)$ is very low, and the corresponding line lies

outside the diagram range.

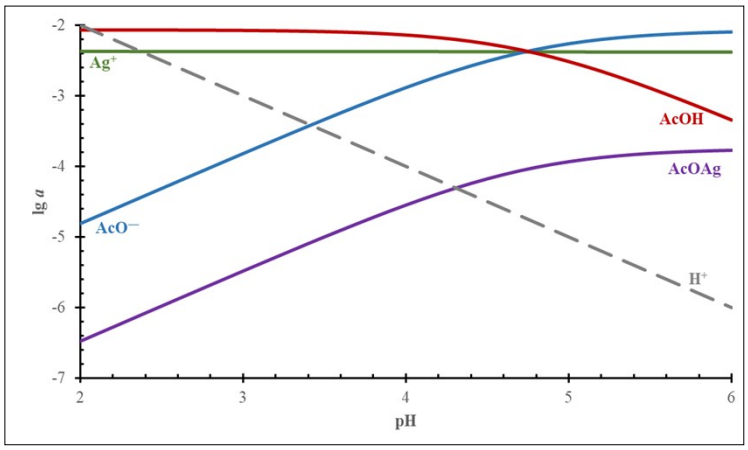

3.5.2. Equilibria involving nickel-acetate complexation

For the equilibria

$$\begin{cases} Ni^{2+}\ (aq) + CH_3COO^-\ (aq) \rightleftharpoons CH_3COONi^+\ (aq), \\ CH_3COONi^+ + CH_3COO^-\ (aq) \rightleftharpoons Ni(CH_3COO)_2\ (aq), \\ H^+\ (aq) + CH_3COO^-\ (aq) \rightleftharpoons CH_3COOH\ (aq) \end{cases}$$

the activities of the species are related to each other according to the following equations:

$$\begin{cases} \dfrac{a_{CH_3COONi^+\ (aq)}}{a_{Ni^{2+}\ (aq)} \cdot a_{CH_3COO^-\ (aq)}} = 23{,}254\ {}^{L}/_{mol}, \\ \dfrac{a_{Ni(CH_3COO)_2\ (aq)}}{a_{CH_3COONi^+\ (aq)} \cdot a_{CH_3COO^-\ (aq)}} = 48{,}067\ {}^{L}/_{mol}, \\ \dfrac{a_{CH_3COOH\ (aq)}}{a_{H^+\ (aq)} \cdot a_{CH_3COO^-\ (aq)}} = 5{,}594 \cdot 10^4\ {}^{L}/_{mol}, \\ a_{Ni^{2+}\ (aq)} + a_{CH_3COONi^+\ (aq)} + a_{Ni(CH_3COO)_2\ (aq)} = 0{,}00279\ {}^{mol}/_{L}, \\ a_{CH_3COOH\ (aq)} + a_{CH_3COO^-\ (aq)} + a_{CH_3COONi^+\ (aq)} + 2 \cdot a_{Ni(CH_3COO)_2\ (aq)} = 0{,}00871\ {}^{mol}/_{L}. \end{cases}$$

The dependencies of thermodynamic activities of ions on pH value are shown on the diagram below.

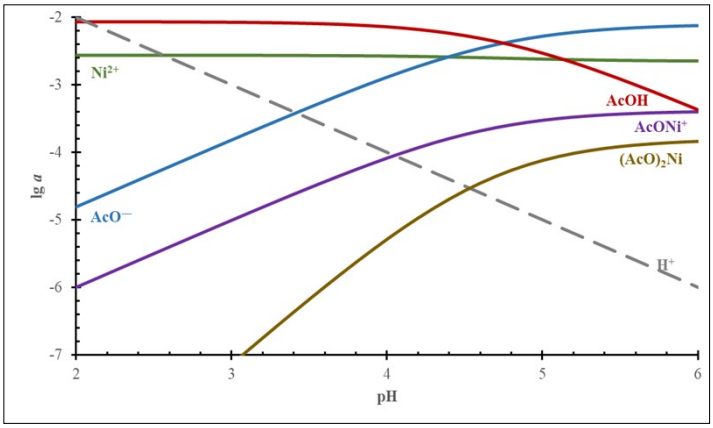

The diagrams in above sections show that at the reaction conditions simple nickel, silver and acetate-ions (or undissociated acetic acid) predominate in a solution, and complex ions are present in very small quantities and do not affect the electrochemical reactions of metals.

3.5.3 Electrochemical equilibria in aqueous solution

The chemical and electrochemical equilibria in the Ni–Ag–NO_3^-–AcO^-–H_2O system were calculated at 298,15 K, air pressure of 1 bar and the activities of nickel, silver, nitrate, and acetate ions in the solution as was calculated in Section 4.4. The diagram is presented below. The partial pressure of methane according to its average atmospheric concentration[1] is equal to $2 \cdot 10^{-6}$ bar. The standard Gibbs energy of formation of nickel hydride Ni_2H was taken from Ref[13]. This shows that at the reaction conditions, no hydrolysis of metal cations or formation of metal oxides occurs. The nickel and silver ions are reduced independently of each other.

4. Details of electrochemical analysis

4.2 Details for the evaluation of electrochemically active surface area (ECSA)

To obtain a relatively accurate electrochemically active surface area (ECSA) value, the actual amount of catalyst on modified GC was quantified by ICP-OES. ECSA of Ag-contained samples was determined by Pb underpotential deposition (Pb_{upd}) stripping method.[14–16] Specifically, the electrolyte solution 0.1 M KOH was purged with N_2 (purity 99.95%) for 30 minutes, thereafter 125 µM $Pb(NO_3)_2$ was added. The potential was held at 0.20 V for Pb underpotential deposition for 300 s and swept to 0.7 V at 10 mV s^{-1}. The area under the Pb_{upd} stripping peak of the stable voltammogram was integrated to calculate the electrochemical surface area using the theoretical Pb_{upd} surface charge on Ag of 280 µC cm^{-2}.[14] The estimated surface area (cm^2) and surface area were then normalized to the mass of Ag ($m^2\ g^{-1}$). ECSA measurements of Ni have been described in our previous work.[17] The hydrogen underpotential deposition (H_{upd}) method[18] was used to measure the ECSA of the commercial Pt/C.

4.3 Koutecky−Levich plots and calculation of electron transfer number.

The ORR measurement was performed in 0.1 M KOH by using a rotating disk electrode (RDE) setup. The ORR kinetics of the freestanding catalysts was investigated by collecting polarization curves at various rotation speeds. Based on those polarization curves, the electron transfer number (n), which reflects the first order ORR kinetics, was then calculated using the Koutecky−Levich (K−L) equation:[19]

$$\frac{1}{i}=\frac{1}{i_k}+\frac{1}{i_d}=\frac{1}{n\cdot F\cdot \kappa\cdot C_0}+\frac{1}{0.2\cdot n\cdot F\cdot C_0\cdot D_0^{2/3}\cdot v^{-1/6}\cdot \omega^{1/2}}$$

Where i is the current density measured experimentally, i_K and i_d represent the kinetic and the limiting diffusion current density, respectively, F is the Faraday constant (96485 C·mol^{-1}), κ is the electrochemical rate constant for O_2 reduction (cm s^{-1}) at a specific potential, C_0 is the dissolved concentration of O_2 (1.2×10^{-6} mol·cm^{-3}), D_0 is the diffusion coefficient of O_2 (1.9×10^{-5} cm^2 s^{-1}), v is the kinetic viscosity of the electrolyte (0.01 cm^2 s^{-1}), and ω is rotating rate (rpm) of the electrode.

5. Introduction of γ-radiation induced synthesis method

Ionizing radiation induced processing is a safe, cost-effective, and environmentally friendly way to produce nanomaterials. The use of radiation in the high frequency range of the electromagnetic spectrum allows direct energy transfer from the source to the final product, thus minimizing the energy losses.[20] A Cs-137 gamma cell setup used in the current study is a self-sustaining system since it does not require an external power source. The instrument is relatively compact, it does not need cooling, and is well shielded. Up to 8 samples can be placed into the chamber and irradiated simultaneously. The sample delivery to the processing position occurs automatically so that the probability of receiving a radiation dose by the user is excluded. Since the radiation induced synthesis is based on redox reactions of ions in precursors solutions with active species, water radiolysis products, the use of potentially harmful reactants (initiators, crosslinking agents, acids, etc.) is minimized. The radiolysis stops immediately (after 10^{-6} s) when the reaction mixture is removed from the radioactive source. Therefore, the number of reacting species, and thus the amount of obtained precipitate, is controlled by the total irradiation dose, which is proportional to the irradiation time with high accuracy. In addition, no temperature control is required during the synthesis procedure. Thus, ionizing radiation induced processes open the possibility for in-situ, one-step, room-temperature production of complex compounds, such as catalysts on supports,[21,22] bi-functional materials,[23] nanostructures in a confined media,[24] etc. Moreover, considering the large penetration depth of γ rays, this method is suitable for the scale-up production of nanomaterials.

Table S1. ***Reduction potential of chemicals involved in the material synthesis.***

Reduction Potential	H_2O/e_{aq}^-	$HO^\bullet/H_2O$	$(CH_3)_2C^\cdot OH/(CH_3)_2CHOH$	Ag^+/Ag^0	Ni^{2+}/Ni^0
E_0 / V(vs *SHE*)	–2.7	+1.8	–1.8	+0.799	–0.257

Table S2. ***Structural parameters of Ag-Ni compounds obtained from XRD and TEM studies***

Catalyst	Composition/morphology	Lattice parameter, a in [Å], from SAED	Lattice parameter, a in [Å] from XRD
		Ag, fcc	Ag, fcc

Ag@NiO	Ag – core; Ni – based - shell (core-shell structure)	4.177±0.018	4.105±0.007
Ag/Ni	Ag large monocrystalline particles and Ni-based small particles forming clusters (heterostructures)	4.175±0.047	4,105±0.007
Ag	Metallic Ag particles having five twinned structure		4.096±0.008

Table S3. ***XRD peak positions indicated in 2θ range from 20° to 45° and corresponding Ag- and Ni-based compounds.***

Ag/Ni		Ag@NiO	
2 Theta	Compound	2 Theta	Compound
27.6	Ni_2O_3[25]	29.6	$Ag(NiO_2)$ (29.2°)[26]
31.9	Ni_2O_3[25]	31.2	N/A
34.0	Ag_6O_2(33.7°)[27];Ag_2O(33.7°)[28]; Ag_2NiO_2 (33.5°)[29]	34.0	Ag_6O_2(2θ=33.7°)[27];Ag_2O(33.7°)[28]; Ag_2NiO_2 (33.5°)[29]
36.2	Ag_6O_2(36.3°)[27], Ag_2O(36.4°)[28]; Ag_2NiO_2 (36.2°)[29]	36.3	Ag_6O_2(2θ=36.3°)[27]; Ag_2O(36.4°)[28]; $Ag(NiO_2)$ (36.1°)[26]; Ag_2NiO_2 (36.2°)[29]
37.9	Ag metal[30]	37.9	Ag metal[30]
44.0	Ag metal[30]	44.1	Ag metal[30]

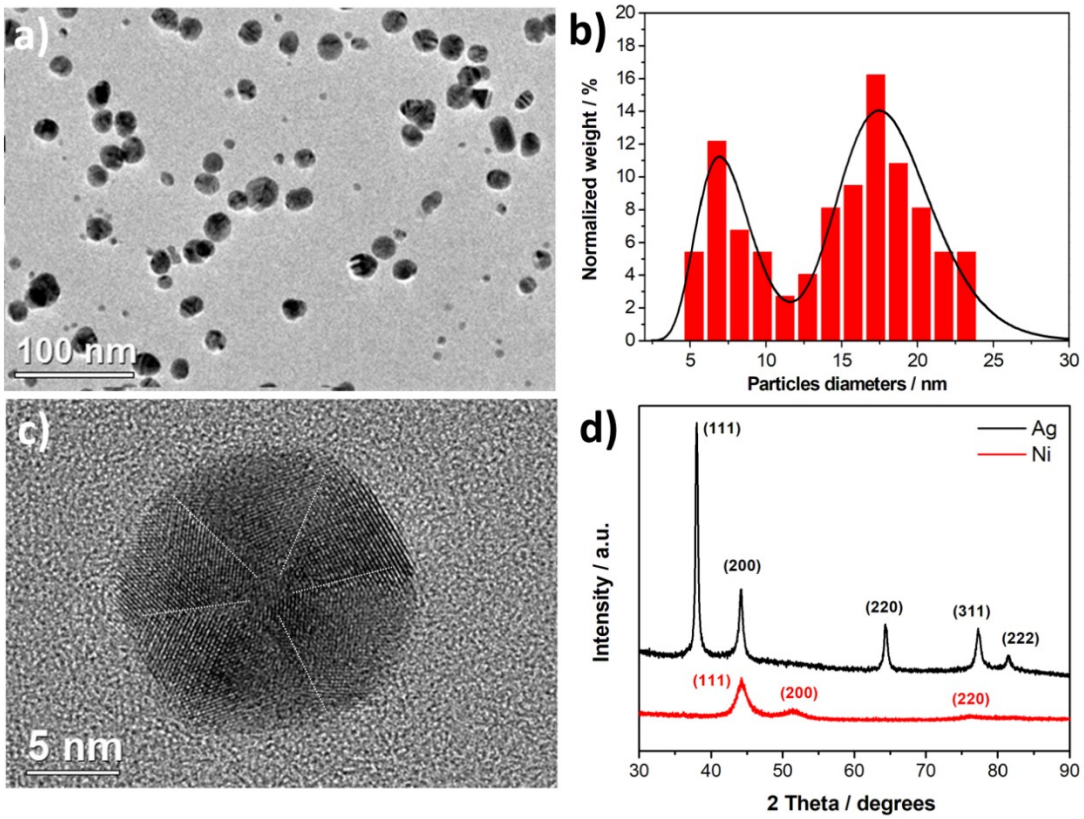

Figure S1 ***a) TEM image of Ag nanoparticles. b) Sizes distribution histogram calculated from TEM images, fitted to lognormal function. c) HRTEM image of Ag nanoparticle, dash lines reveal the stacking faults and five-fold twined structure. d) XRD patterns of Ag and Ni, Miller indices of corresponding planes in fcc Ag and fcc Ni are labeled.***

X-ray diffraction studies performed on the synthesized Ag nanoparticles reveal that the obtained precipitate consists of *fcc* Ag (Figure S1d). The lattice constant calculated from XRD pattern is a = 4.096 ± 0.008 Å, which is slightly larger than that for the bulk Ag (a = 4.086 Å).[30] The Ag precipitate consists of spherical particles which diameters follow a bimodal size distribution where the smaller particles, with the average size of 7.4 ± 1.6 nm co-exist stably with the larger ones with average diameters 18.0 ± 2.5 nm (Figure S1a, 1b). The particles size distribution fitted to a lognormal function is shown in Figure S1b. Such a bimodal ensemble may occur in solutions containing surfactants (in our case, it is PVA) and is attributed to the difference in interaction energies of polymers with particles that have different diameters.[31] The obtained Ag nanoparticles show five-fold twinned morphology (Figure S1c). These structures are often noticeable in *fcc* noble metals.[32–34] The shape of such crystals can be described as five single crystal *fcc* subunits sharing their {111} planes[35] and leads to a lattice strain and surface defects. Both defects types may contribute to the enhanced ORR activity of the catalyst.[36–38]

Ni nanoparticles were synthesized from Ni acetate aqueous solution in the form of a black precipitate. In Figure S1d, an X-ray diffractogram recorded from the obtained Ni precipitate is presented. As seen in the figure, the XRD pattern contains peaks that belong only to *fcc* Ni, no other XRD peaks are present, indicating the absence of any other crystalline phases in the precipitate. Thus, one can assume that the synthesized material contains mainly metallic *fcc* Ni.

The detailed description structure, composition, morphology, magnetic and electrochemical properties of the metallic Ni nanoparticles obtained by the γ-radiation induced synthesis is provided in our previous study. As reported, Ni precipitate consists of metallic Ni nanoparticles with diameters of about 3 nm agglomerated to larger clusters. The cluster sizes are between 15 and 40 nm. The surfaces of Ni agglomerates are covered with $NiO/Ni(OH)_2$ poor-crystalline/amorphous layers.[17]

Table S4. Binding energies (BE) of O, Ag and Ni core levels measured with XPS on Ag, Ag@NiO core-shell and Ag/Ni heterostructure nanocatalysts. Numbers in brackets are the calculated molar percentage of corresponding species.

	Ag BE, eV	Ag@NiO BE, eV	Ag/Ni BE,eV	Possible Compounds
O 1s		529.8	529.9	Ni-O; Ni-OOH, Ag-O[39]
		531.4	531.5	Ag-O, Ni-O, Ni-OH
	532.1			O adsorbed[40], Ag-O[41], Ag-OH[42]
	532.8	532.5	532.6	Adsorbed H_2O[41]
Ag	368.2 **(50%)**			Ag(I); AgO_x[39]
$3d_{5/2}$	368.8 **(50%)**			Ag (0) metal[43]
	371.5			Plasmon-loss satellite[44]
	374.2			
	374.8			
$3d_{3/2}$	377.4			
Ag		368.2 **(17 %)**		Ag (0)[40]
$3d_{5/2}$		368.6 **(19 %)**		Ag in Ag-Ni compounds[45,46]
		371.5		Plasmon-loss satellite
		374.2		
$3d_{3/2}$		374.6		
		377.4		
Ag			367.9 **(32 %)**	Ag (I) (Ag_2O)[40]
$3d_{5/2}$			368.2 **(30 %)**	Ag (0)[40]
			371.5	Plasmon-loss satellite
			373.9	
$3d_{3/2}$			374.2	
			377.4	
Ni $2p_{3/2}$		854.7; 856.5 **(64 %)**		Ni (II) multiplet (NiO)[47]
		859.6; 862.5		Shake-up satellites[48]

$2p_{1/2}$		872.4; 874.2 877.6; 881.0		
Ni $2p_{3/2}$ **$2p_{1/2}$**			852.4 **(4 %)** 854.3; 856.5 **(34 %)** 859.4; 863.1 869.7 871.8; 874 877.6; 881.8	Ni^0 (metal)[49] Ni(II)/Ni(III)[50] Shake-up satellites[48]

XPS analysis of Ag nanoparticles: As reported in the literature, the binding energy (BE) that corresponds to Ag $3d_{5/2}$ spectral line is 368.1 eV for bulk Ag.[40] For bulk Ag_2O, this energy is shifted towards lower values, 367.7 eV.[40] In nanomaterials, such as thin films, nanoparticles, atomic clusters and others, Ag $3d_{5/2}$ BE levels for both Ag^0 and Ag^+ tend to shift towards higher values due to changes in the electronic structure, by 0.4-0.8 eV.[39,41,51–53] Deconvolution of the Ag 3d spectral lines performed in the current study reveals binding energies of 368.8 and 368.2 eV for the Ag $3d_{5/2}$, which may correspond to Ag^0 and Ag^+, respectively. However, both values are higher as compared to those for the bulk metallic Ag and Ag_2O. Since the BE shift is rather large, an unambiguous interpretation of the spectra is difficult. Therefore, the results from the structural studies should be considered here. The shift in BE may be partially attributed to the size effect since the studied Ag sample consists of nanoparticles that have bi-modal size distribution with average diameters of 7.4 nm and 18.0 nm.[43] So far, as the sizes of the nanoparticles presented in our study are still too large to significantly affect the energy of core-level electrons,[54] other factors are to be considered. Thus, as shown by structural analysis, Ag nanoparticles possess a five-fold twinned morphology, which may lead to an induced tensile strain that may, in turn, contribute to the BE shift towards higher values. Thus, Ag nanoparticles consist of metallic Ag with Ag_2O formed at the surface. Another possibility is the formation of non-stoichiometric surface and sub-surface Ag-O compounds. The latter statement is supported by the fact that oxygen signal at 532.1 eV may correspond to the BE for the adsorbed/absorbed oxygen on the Ag surface.[40,55] Note that the existence of AgO can be neither confirmed nor disproved since AgO may be reduced by the X-ray beam. The existence of Ag^0 in all studied samples is further confirmed by the presence of plasmon-loss structures at 371.5 and 377.4 eV which are exclusive to metallic Ag.[44,55]

Table S5. ***Ag, Ni stoichiometric ratio, the metal amount on the electrode (m_{GC}) after electrochemical test, and the calculated ECSA based on the data from Pb-stripping and ICP-OES. ECSA of Ni was measured and calculated by the double-layer capacitance (C_{dl}) method, hydrogen underpotential deposition (H_{upd}) method was used to measure the ECSA of commercial Pt/C.***

Catalyst	Ag_xNi_y	m_{GC}	ECSA	
			cm^2	$m^2 g^{-1}$
Ag	/	10 μg $_{Ag}$	4.4	43.6
Ag@NiO	Ag_4Ni_1	18 μg $_{Ag}$	5.5	30.4
Ag/Ni	Ag_3Ni_1	11 μg $_{Ag}$	4.6	41.9
Ni	/	50 μg $_{Ni}$	19.6	39.2
Pt/C	/	2 μg $_{Pt}$	0.9	43.1

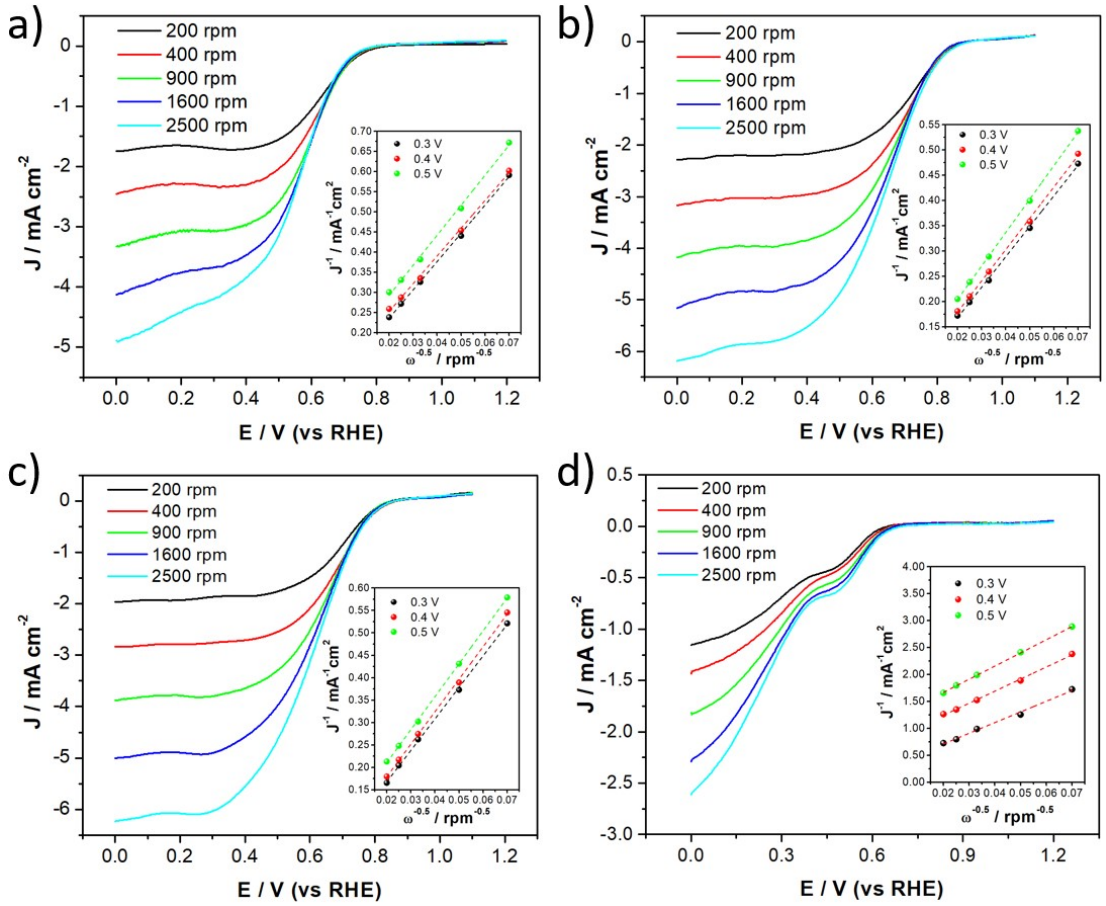

Figure S2. ***ORR Polarization curves of Ag (a), Ag@NiO (b), Ag/Ni (c) and Ni (d) obtained in O_2-saturated 0.1 M KOH at five different rotation speed with K–L plots insert at 0.3 V, 0.4 V and 0.5 V respectively.***

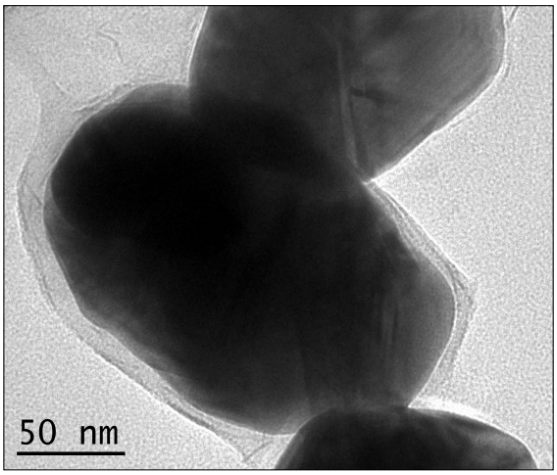

Figure S3. ***Typical Ag@NiO nanoparticles covered with surfactant PVA (layer with light color) on the surface.***

Reference

1 Q. Schiermeier, *Nature*, 2020. (https://doi.org/10.1038/d41586-020-02116-8)

2 B. Baranowski and K. Bocheńska, *Zeitschrift fur Phys. Chemie*, 1965, **45**, 140–152.

3 X. J. Liu, F. Gao, C. P. Wang and K. Ishida, *J. Electron. Mater.*, 2008, **37**, 210–217.

4 O. Redlich and A. T. Kister, *Ind. Eng. Chem.*, 1948, **40**, 345–348.

5 T. Sörgel and M. Jansen, *J. Solid State Chem.*, 2007, **180**, 8–15.

6 H. Gamsjäger, F. J. Mompean, Issy-les-Moulineaux (France), NEA Data Bank. and OECD Nuclear Energy Agency., *Chemical thermodynamics of nickel*, 2005.

7 G. K. Schweitzer and L. L. Pesterfield, *The Aqueous Chemistry of the Elements*, Oxford University Press, USA, 2010.

8 P. Brown and C. Ekberg, in *Kinetics of Inorganic Reactions*, Elsevier, 1966, p. 280.

9 D. D. Wagman, W. H. Evans, V. B. Parker, R. H. Schumm, I. Halow, S. M. Bailey, K. L. Churney and R. L. Nuttall, *J. Phys. Chem. Ref. Data*, 1989, 18, 1807–1812.

10 P. Debye and E. Huckel, *Phys. Zeitschrift*, 1923, **24**, 185–206.

11 J. Kielland, *J. Am. Chem. Soc.*, 1937, **59**, 1675–1678.

12 *CRC Handbook of Chemistry and Physics, 93rd Edition*, CRC Press, 2016.

13 B. Baranowski and K. Bocheńska, *Zeitschrift fur Phys. Chemie*, 1965, **45**, 140–152.

14 A. Holewinski, J. C. Idrobo and S. Linic, *Nat. Chem.*, 2014, **6**, 828–834.

15 G. K. H. Wiberg, K. J. J. Mayrhofer and M. Arenz, *Fuel Cells*, 2010, **10**, 575–581.

16 G. Wiberg, K. Mayhofer and M. Arenz, *ECS Trans.*, 2019, **19**, 37–46.

17 Y. Yang, M. Johansson, A. Wiorek, N. V. Tarakina, F. Sayed, R. Mathieu, M. Jonsson and I. L. Soroka, *Dalt. Trans.*, 2021, **50**, 376–383.

18 F. J. Vidal-Iglesias, R. M. Arán-Ais, J. Solla-Gullón, E. Herrero and J. M. Feliu, *ACS Catal.*, 2012, **2**, 901–910.

19 A. L. Ong, K. K. Inglis, D. K. Whelligan, S. Murphy and J. R. Varcoe, *Phys. Chem. Chem. Phys.*, 2015, **17**, 12135–12145.

20 A. J. Berejka, *Radiat. Phys. Chem.*, 1995, **46**, 429–437.

21 I. L. Soroka, N. V. Tarakina, A. Hermansson, L. Bigum, R. Widerberg, M. S. Andersson, R. Mathieu, A. R. Paulraj and Y. Kiros, *Dalt. Trans.*, 2017, **46**, 9995–10002.

22 I. L. Soroka, J. Bjervås, J. Ceder, G. Wallnerström, M. Connan, N. V. Tarakina, A. C. Maier and Y. Kiros, *Radiat. Phys. Chem.*, 2020, **169**, 108370.

23 J. Belloni, M. Mostafavi, H. Remita, J. L. Marignier and M. O. Delcourt, *New J. Chem.*, 1998, **22**, 1239–1255.

24 K. Guo, L. J. Rowland, L. H. Isherwood, G. Glodan and A. Baidak, *J. Mater. Chem. A*, 2020, **8**, 714–723.

25 P. S. Aggarwal and A. Goswami, *J. Phys. Chem.*, 1961, **65**, 2105–2105.

26 T. Sörgel and M. Jansen, *Zeitschrift für Anorg. und Allg. Chemie*, 2005, **631**, 2970–2972.

27 W. Beesk, P. G. Jones, H. Rumpel, E. Schwarzmann and G. M. Sheldrick, *J. Chem. Soc. Chem. Commun.*, 1981, 664.

28 S. S. Kabalkina, S. V. Popova, N. R. Serebryanaya and L. F. Vereshchagin, *Dokl. Akad. Nauk SSSR*, 1963, **152**, 853–854.

29 D. A. Svintsitskiy, M. K. Lazarev, T. Y. Kardash, E. A. Fedorova, E. M. Slavinskaya and A. I. Boronin, *J. Chem. Phys.*, 2020, **152**, 044707.

30 E. R. Jette and F. Foote, *J. Chem. Phys.*, 1935, **3**, 605–616.

31 C. Y. Shih, R. Streubel, J. Heberle, A. Letzel, M. V. Shugaev, C. Wu, M. Schmidt, B. Gökce, S. Barcikowski and L. V. Zhigilei, *Nanoscale*, 2018, **10**, 6900–6910.

32 R. Majee, A. Kumar, T. Das, S. Chakraborty and S. Bhattacharyya, *Angew. Chemie Int. Ed.*, 2020, **59**, 2881–2889.

33 T. Liu, P. Jiang, Q. You and S. Ye, *CrystEngComm*, 2013, **15**, 2350–2353.

34 S. Liu, X. Mu, W. Li, M. Lv, B. Chen, C. Chen and S. Mu, *Nano Energy*, 2019, **61**, 346–351.

35 Y. Sun, Y. Ren, Y. Liu, J. Wen, J. S. Okasinski and D. J. Miller, *Nat. Commun.*, 2012, **3**, 1–6.

36 S. Liu, Q. Zhang, Y. Li, M. Han, L. Gu, C. Nan, J. Bao and Z. Dai, *J. Am. Chem. Soc.*, 2015, **137**, 2820–2823.

37 H. Erikson, A. Sarapuu and K. Tammeveski, *ChemElectroChem*, 2019, **6**, 73–86.

38 E. M. Dietze and H. Grönbeck, *ChemPhysChem*, 2020, **21**, 2407–2410.

39 N. J. Firet, M. A. Blommaert, T. Burdyny, A. Venugopal, D. Bohra, A. Longo and W. A. Smith, *J. Mater. Chem. A*, 2019, **7**, 2597–2607.

40 G. Schön, J. Tummavuori, B. Lindström, C. R. Enzell, C. R. Enzell and C.-G. Swahn, *Acta Chem. Scand.*, 1973, **27**, 2623–2633.

41 Y. Y. Chen, S. H. Yu, Q. Z. Yao, S. Q. Fu and G. T. Zhou, *J. Colloid Interface Sci.*, 2018, **510**, 280–291.

42 P. Prieto, V. Nistor, K. Nouneh, M. Oyama, M. Abd-Lefdil and R. Díaz, *Appl. Surf. Sci.*, 2012, **258**, 8807–8813.

43 I. Lopez-Salido, D. C. Lim and Y. D. Kim, *Surf. Sci.*, 2005, **588**, 6–18.

44 J. Leiro, E. Minni and E. Suoninen, *J. Phys. F Met. Phys.*, 1983, **13**, 215–221.

45 S. Lv, F. Yang, X. Chu, H. Wang, J. Yang, Y. Chi and X. Yang, *Metals (Basel).*, 2019, **9**, 826.

46 F. Bao, F. Tan, W. Wang, X. Qiao and J. Chen, *RSC Adv.*, 2017, **7**, 14283–14289.

47 K. S. Kim and N. Winograd, *Surf. Sci.*, 1974, **43**, 625–643.

48 P. Dubey, N. Kaurav, R. S. Devan, G. S. Okram and Y. K. Kuo, *RSC Adv.*, 2018, **8**, 5882–5890.

49 P. T. Andrews, T. Collins and P. Weightman, *J. Phys. C Solid State Phys.*, 1981, **14**, L957.

50 M. C. Biesinger, B. P. Payne, A. P. Grosvenor, L. W. M. Lau, A. R. Gerson and R. S. C. Smart, *Appl. Surf. Sci.*, 2011, **257**, 2717–2730.

51 L. Shi, L. Liang, J. Ma, F. Wang and J. Sun, *Catal. Sci. Technol.*, 2014, **4**, 758–765.

52 E. Sumesh, M. S. Bootharaju, Anshup and T. Pradeep, *J. Hazard. Mater.*, 2011, **189**, 450–457.

53 J. F. Weaver and G. B. Hoflund, *Chem. Mater.*, 1994, **6**, 1693–1699.

54 R. Dietsche, D. C. Lim, M. Bubek, I. Lopez-Salido, G. Ganteför and Y. D. Kim, *Appl. Phys. A Mater. Sci. Process.*, 2008, **90**, 395–398.

55 G. B. Hoflund, Z. F. Hazos and G. N. Salaita, *Phys. Rev. B*, 2000, **62**, 11126–11133.